



**HAL**  
open science

# Formation and Physical Properties of (NbTa)<sub>67</sub>(HfZr)<sub>33</sub> Medium-Entropy Alloy and (NbTa)<sub>67</sub>(HfZrTi)<sub>33</sub> High-Entropy Alloy Prepared by Mechanical Alloying

Rafal Idczak, Piotr Sobota, Daniel Gnida, Slawomir Kolodziej, Beata Chrzaszcz, Mathieu Pasturel, Adam Pikul

## ► To cite this version:

Rafal Idczak, Piotr Sobota, Daniel Gnida, Slawomir Kolodziej, Beata Chrzaszcz, et al.. Formation and Physical Properties of (NbTa)<sub>67</sub>(HfZr)<sub>33</sub> Medium-Entropy Alloy and (NbTa)<sub>67</sub>(HfZrTi)<sub>33</sub> High-Entropy Alloy Prepared by Mechanical Alloying. Metallurgical and Materials Transactions A, 2024, 10.1007/s11661-024-07489-3 . hal-04651825

**HAL Id: hal-04651825**

**<https://hal.science/hal-04651825>**

Submitted on 17 Jul 2024

**HAL** is a multi-disciplinary open access archive for the deposit and dissemination of scientific research documents, whether they are published or not. The documents may come from teaching and research institutions in France or abroad, or from public or private research centers.

L'archive ouverte pluridisciplinaire **HAL**, est destinée au dépôt et à la diffusion de documents scientifiques de niveau recherche, publiés ou non, émanant des établissements d'enseignement et de recherche français ou étrangers, des laboratoires publics ou privés.



Distributed under a Creative Commons Attribution 4.0 International License

# Formation and Physical Properties of $(\text{NbTa})_{0.67}(\text{HfZr})_{0.33}$ Medium-Entropy Alloy and $(\text{NbTa})_{0.67}(\text{HfZrTi})_{0.33}$ High-Entropy Alloy Prepared by Mechanical Alloying



RAFAŁ IDCZAK, PIOTR SOBOTA, DANIEL GNIDA, SŁAWOMIR KOŁODZIEJ, BEATA CHRZĄSZCZ, MATHIEU PASTUREL, and ADAM PIKUL

The medium-entropy alloy  $(\text{NbTa})_{0.67}(\text{HfZr})_{0.33}$  and the high-entropy alloy  $(\text{NbTa})_{0.67}(\text{HfZrTi})_{0.33}$  were prepared by mechanical alloying using high-energy planetary ball mill. The results of X-ray diffraction, scanning electron microscopy, and positron annihilation lifetime spectroscopy measurements suggest that both as-prepared powders are multicomponent alloys in amorphous (or highly disordered) state. The magnetic and thermodynamic results obtained for these powders undoubtedly prove that bulk superconductivity is not observed at temperatures exceeding 2 K. Thermal treatment of both studied materials leads to decomposition of the amorphous phase and precipitation of several crystalline phases. In both annealed samples, the structure of the main crystalline phase was identified as body-centered cubic (bcc), and in this phase, bulk superconductivity was observed below 6.5 K.

<https://doi.org/10.1007/s11661-024-07489-3>  
© The Author(s) 2024

## I. INTRODUCTION

MEDIUM-ENTROPY alloys (MEAs) and high-entropy alloys (HEAs) are, by arbitrary definition, single-phase solid solutions composed of elements with a molar fraction of 5 to 35 atomic pct. In fact, the main defining factor is the configurational entropy value ( $\Delta S_{\text{config}}$ ), which is at least partly responsible for stabilizing a single-phase structure. For MEAs,  $\Delta S_{\text{config}}$  lies between 0.69 and 1.61  $R$ , while for HEAs  $\Delta S_{\text{config}} \geq 1.61 R$  ( $R$  is a gas constant).<sup>[1–3]</sup> So far, it has been widely proven that both MEAs and HEAs have excellent specific strength, superior mechanical performance at high temperatures, and fracture toughness at low

temperatures.<sup>[2]</sup> According to Yeh *et al.*,<sup>[1]</sup> these exceptional properties are caused by the following effects: thermodynamic stabilization of the single phase with the high-entropy effect, retardation of the growth of the second phase from the single-phase solution by the slowed diffusion, excessive strength and slow kinetics due to strong lattice distortions, and the so-called cocktail effect.

In 2014, the first HEA superconductor with the composition  $\text{Ta}_{0.34}\text{Nb}_{0.33}\text{Hf}_{0.08}\text{Zr}_{0.14}\text{Ti}_{0.11}$  (in at. pct) was found,<sup>[4]</sup> revealing a new facet of the capabilities. A variety of studies have been performed on HEA superconductors since that time, aiming to designate their potential for practical applications. In particular, the occurrence of bulk superconductivity in HEAs which also display excellent mechanical properties at cryogenic temperatures makes them promising candidates for superconducting magnets.<sup>[5]</sup> Additionally, in the case of many HEA superconductors which are composed of transition metals, the multicomponent phase, stabilized by the high configurational entropy, appears to fall between an ordered solid and an amorphous material. Therefore, HEAs can be treated as excellent intermediate systems for studying superconductivity on a fundamental level.<sup>[5,6]</sup>

Up to the present time, MEA and HEA superconductors are fabricated primarily through high-temperature arc-melting technique.<sup>[6,7]</sup> A promising alternative for this method is mechanical alloying (MA). MA is a solid-state powder-processing technique involving

RAFAŁ IDCZAK is with the Institute of Experimental Physics, University of Wrocław, pl. M. Borna 9 50-204, Wrocław, Poland. Contact e-mail: rafal.idczak@uwr.edu.pl PIOTR SOBOTA is with the Institute of Experimental Physics, University of Wrocław and also with the Institute of Low Temperature and Structural Research, Polish Academy of Sciences, ul. Okólna 2 50-422, Wrocław, Poland. DANIEL GNIDA and ADAM PIKUL are with the Institute of Low Temperature and Structural Research, Polish Academy of Sciences. SŁAWOMIR KOŁODZIEJ and BEATA CHRZĄSZCZ are with the Institute of Materials Engineering, University of Silesia in Katowice, ul. 75 Pułku Piechoty 1A 41-500, Chorzów, Poland. MATHIEU PASTUREL is with the Institut des Sciences Chimiques de Rennes, Univ Rennes, CNRS, UMR 6226 35042, Rennes, France. Manuscript submitted January 31, 2024; accepted June 13, 2024.

repeated cold welding, fracturing, and re-welding of powder particles in a high-energy ball mill. The key benefits provided by MA are enhanced solid solubility, room temperature processing, and homogenous alloy formation.<sup>[8]</sup> Kumar *et al.* in their review work,<sup>[9]</sup> provide the list of MEAs and HEAs synthesized by MA. Unfortunately, there is no information about superconducting properties of these materials. For this reason, we decided to prepare MEA  $(\text{NbTa})_{0.67}(\text{HfZr})_{0.33}$  and HEA  $(\text{NbTa})_{0.67}(\text{HfZrTi})_{0.33}$  via MA. We choose these two alloys since their superconducting properties for the samples prepared by arc-melting method are well known. In the case of  $(\text{NbTa})_{0.67}(\text{HfZr})_{0.33}$ , the superconducting transition temperature  $T_c = 6.6$  K, while for  $(\text{NbTa})_{0.67}(\text{HfZrTi})_{0.33}$ ,  $T_c = 7.6$  K.<sup>[5,7]</sup>

The present work reports on the synthesis and detailed study of physical properties of  $(\text{NbTa})_{0.67}(\text{HfZr})_{0.33}$  and  $(\text{NbTa})_{0.67}(\text{HfZrTi})_{0.33}$  alloys prepared by MA. In particular, the crystal structure, chemical composition, and homogeneity of the samples of the as-milled, thermally treated, and SPS-sintered powders are characterized by X-ray diffraction (XRD), scanning electron microscopy (SEM), and positron annihilation lifetime spectroscopy (PALS). The magnetic and thermodynamic properties of the as-milled samples were determined down to 1.8 K. The obtained results are discussed and compared with corresponding data which were previously reported for  $(\text{NbTa})_{0.67}(\text{HfZr})_{0.33}$  and  $(\text{NbTa})_{0.67}(\text{HfZrTi})_{0.33}$  alloys prepared by arc-melting method.<sup>[3,7]</sup>

## II. EXPERIMENTS AND DATA ANALYSIS

The  $(\text{NbTa})_{0.67}(\text{HfZr})_{0.33}$  and  $(\text{NbTa})_{0.67}(\text{HfZrTi})_{0.33}$  alloys were synthesized by the mechanical alloying (MA) using a PULVERISETTE 6 planetary ball mill (Fritsch) at room temperature. Commercially available mesh  $\sim 325$  powders of Nb (99.97 pct, Alfa Aesar), Ta (99.6 pct, Alfa Aesar), Ti (99.99 pct, Alfa Aesar), Zr (99.5 pct, Goodfellow), and Hf (99.6 pct, Thermo Scientific) were used as starting materials.

The metal powders of total mass 10 g were placed in tungsten carbide (WC) vial with 25 WC grinding balls. Weight ratio of balls to powder was close to 10 to 1. Sealed vial was purged with argon gas to remove air. Milling was carried out for 20 hours at 300 RPM. For each 12 minutes of milling, there was 30 minutes of rest to prevent vial overheating and oxidation of powders, so whole synthesis process took 70 hours. Yields of powders after the MA were  $\sim 75$  pct for  $(\text{NbTa})_{0.67}(\text{ZrHf})_{0.33}$  and  $\sim 80$  pct for  $(\text{NbTa})_{0.67}(\text{HfZrTi})_{0.33}$ .

The powders were separated into portions. One portion of the as-milled powders was annealed in the furnace at 1273 K for 24 hours under dynamic vacuum better than  $9 \times 10^{-5}$  mbar. The other portion has undergone Spark Plasma Sintering (SPS) process using FCT HP-D-10 apparatus. Powders were placed in  $\phi = 10$  mm graphite die and sintered at 1273 K and 66 MPa with dwell time of 24 minutes. Temperature was controlled by frontal thermocouple. Heating rate was

100 K/min. After polishing, obtained disks were 1 mm thick.

X-ray powder diffraction (XRD) patterns of the powders and pellets were collected using a PANalytical X'Pert Pro diffractometer with  $\text{CuK}\alpha$  radiation. The obtained patterns were refined and analyzed by the Rietveld method using the FULLPROF software package.<sup>[10]</sup> The morphology and homogeneity of the samples were verified by energy-dispersive X-ray spectroscopy (EDXS) using a FESEM FEI Nova NanoSEM 230 scanning electron microscope equipped with an EDAX Genesis XM4 spectrometer.

The positron annihilation lifetime spectroscopy (PALS) measurements were realized on a standard fast-fast coincidence spectrometer in a 50 ns time scale. The radioactive source used in the measurements was the  $^{22}\text{Na}$  isotope enveloped by two 7.6- $\mu\text{m}$ -thick Kapton foils. The activity of the source was approximately 350 kBq. The investigated powder was poured into two 2-mm-thick 20 mm aluminum hollow disks, forming 1 mm thick and 10 mm in diameter circular samples. The samples were additionally sealed with an additional 7.6- $\mu\text{m}$ -thick sheet of Kapton foil to preserve the samples and the positron source from moisture. The measurements were performed in normal conditions in sandwich geometry with the positron source placed between the two samples, ensuring that all emitted positrons annihilate in the material under investigation. Collected annihilation spectra of at least  $6 \times 10^6$  counts were recorded using the multi-channel pulse amplitude analyzer TUKAN 8k developed by the National Centre for Nuclear Research Poland. The obtained PALS spectra were analyzed using the LT-9.0 software of Kansy,<sup>[11]</sup> taking into account the correction for positron annihilation in the source setting.

The magnetic properties of the alloys were studied using commercial Quantum Design SQUID magnetometer MPMS XL at temperatures down to 1.8 K and in magnetic fields up to 70 kOe. The heat capacity of the as-milled powders pressed into pellets was measured down to 1.8 K using a Quantum Design PPMS platform.

## III. RESULTS AND DISCUSSION

### A. Microstructure and Chemical Composition

Figure 1 shows the XRD patterns collected for the as-milled  $(\text{NbTa})_{0.67}(\text{HfZr})_{0.33}$  and  $(\text{NbTa})_{0.67}(\text{HfZrTi})_{0.33}$  powders. In both cases, the analysis of XRD patterns by Rietveld refinement reveals the presence of two phases. Firstly, one can observe sharp and narrow diffraction peaks which can be attributed to the presence of a small amount of WC ( $< 4$  wt pct) with a hexagonal structure and lattice parameters  $a = 2.90(1)$  Å and  $c = 2.83(1)$  Å (see the lower green ticks in Figure 1). Taking into account the fact that prepared powders do not contain tungsten atoms, it is clear that the presence of this impurity phase is connected with the abrasion of the vial and grinding balls which are made of WC. It should be noted that tungsten carbide impurity introduced by

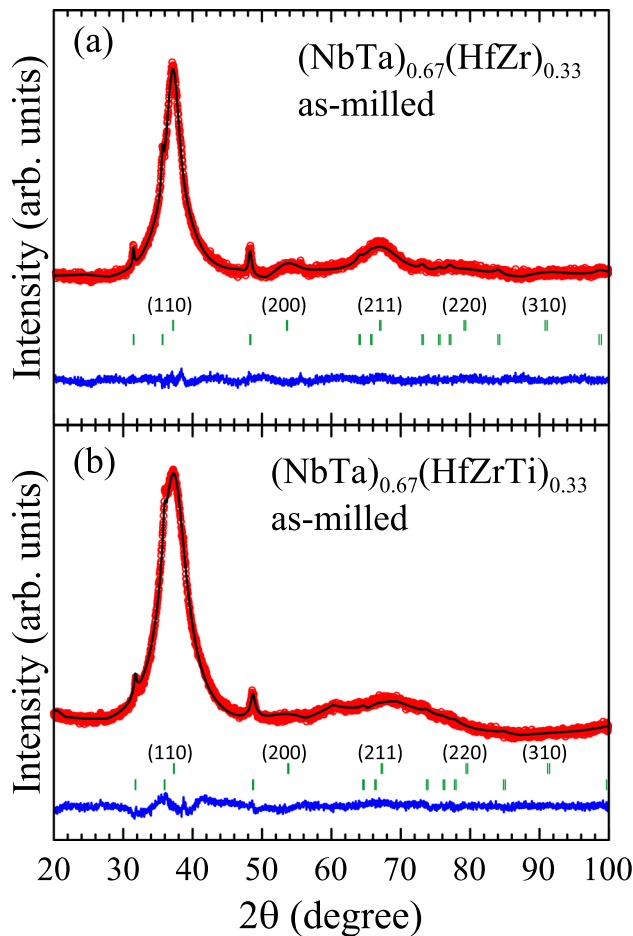


Fig. 1—X-ray diffraction patterns of the as-milled (a)  $(\text{NbTa})_{0.67}(\text{HfZr})_{0.33}$  and (b)  $(\text{NbTa})_{0.67}(\text{HfZrTi})_{0.33}$  powders. Red dots and black lines represent experimental data and results of the Rietveld refinement, respectively, and blue lines show the difference between the two. Green dashes indicate positions of the Bragg reflections described by the corresponding Miller indices (only for bcc phase) (Color figure online).

ball-milling process was also detected in high-entropy carbides which were prepared in similar conditions.<sup>[12]</sup> The second phase is connected with two broad diffraction peaks around  $2\theta = 37$  and  $67$  deg. Since both studied alloys crystallize in body-centered cubic (bcc) when they are synthesized by the arc-melting method,<sup>[5,7]</sup> it is plausible to assume that the positions of these peaks are related to Miller indices of (110) and (211) planes of bcc lattice (space group  $Im\bar{3}m$ ). Accepting this interpretation, the lattice parameter  $a$  determined by Rietveld refinement is  $3.421(2)$  Å for  $(\text{NbTa})_{0.67}(\text{HfZr})_{0.33}$  and  $3.411(1)$  Å for  $(\text{NbTa})_{0.67}(\text{HfZrTi})_{0.33}$ . It is noteworthy that these values are much higher than  $a = 3.36$  Å determined for well-crystallized  $(\text{NbTa})_{0.67}(\text{HfZrTi})_{0.33}$  alloy prepared by arc melting.<sup>[4]</sup> An alternative explanation could be the formation of the amorphous phase during the mechanical alloying process. The XRD patterns reported for fully amorphous equimolar PdPtCuNiP,<sup>[13]</sup> TiZrCuNiBe,<sup>[14]</sup> FeCrSiNb,<sup>[15]</sup> and AlTiVNb<sup>[16]</sup>

multicomponent alloys consist of broad halo peaks without the distinct sharp peaks of the crystalline phase. In fact, the patterns presented in Figure 1 are comparable to those reported in works.<sup>[13–16]</sup>

The XRD patterns obtained for the  $(\text{NbTa})_{0.67}(\text{HfZr})_{0.33}$  and  $(\text{NbTa})_{0.67}(\text{HfZrTi})_{0.33}$  powders after SPS process at 1273 K and 66 MPa with dwell time of 24 minutes, and after annealing in vacuum furnace at 1273 K for 24 hours are presented in Figure 2. As one can notice, the XRD patterns collected for thermally treated powders are much different than those obtained for the as-milled ones (Figure 1). Only sharp peaks which correspond to reflections from crystalline phases are observed indicating that thermal treatment of both as-milled samples leads to decomposition of the amorphous phase. Similar effect was observed in the case of amorphous HEAs PdPtCuNiP<sup>[13]</sup> and TiZrCuNiBe.<sup>[14]</sup>

The analysis of XRD pattern for  $(\text{NbTa})_{0.67}(\text{HfZr})_{0.33}$  after SPS [Figure 2(a)] by Rietveld refinement reveals that the crystal structure of the main crystalline phase (67(1) wt pct) is bcc with  $a = 3.31(1)$  Å. Using the Scherrer equation, the estimated mean crystallite size  $L$  is close to  $22(1)$  nm. The secondary phases are identified as medium-entropy oxide with a rock-salt structure (space group  $Fm\bar{3}m$ , 15(1) wt pct), Hf-Zr mixed dioxide (space group  $P2_1/c$ , 6(1) wt pct), W particles (space group  $Im\bar{3}m$ , 3(1) wt pct), and Zr particles (space group  $P6_3/mmc$ , 9(1) wt pct). In the case of  $(\text{NbTa})_{0.67}(\text{HfZr})_{0.33}$  after vacuum annealing [Figure 2(b)], the phase composition is quite similar to the SPS sample. However, it should be mentioned that the sharper and narrower diffraction peaks indicate better crystallinity of the annealed sample. Consequently, the mean crystallite size determined for the main bcc phase is close to  $L = 149(17)$  nm.

Figure 2(c) presents XRD pattern obtained for  $(\text{NbTa})_{0.67}(\text{HfZrTi})_{0.33}$  powders after SPS process. The major peaks can be indexed to bcc phase with  $a = 3.30(1)$  Å,  $L = 10(1)$  nm, and 49(1) wt pct. The secondary phases are identified as Hf-Zr mixed dioxide (space group  $P2_1/c$ , 9(1) wt pct), W particles (space group  $Im\bar{3}m$ , 2(1) wt pct), and high-entropy oxide with a  $\text{Ti}_3\text{O}$  structure (space group  $P\bar{3}1c$ , 40(1) wt pct). The results obtained for the powder after annealing process [Figure 2(d)] indicate that the sample is composed of the same four phases as the SPS one. Again, the sharper and narrower peaks observed for the annealed sample are associated with the higher crystallinity level in comparison to powder after SPS. The content of main bcc phase is lower for annealed sample and close to 41 wt pct, while  $L = 40(4)$  nm. Finally, it should be noted that the presence of metal oxides in SPS and annealed samples is probably connected with the fact that before thermal treatment the as-milled powders had direct contact with atmospheric gases.

The SEM micrographs with EDXS elemental maps of the as-milled and annealed powders of  $(\text{NbTa})_{0.67}(\text{HfZr})_{0.33}$  and  $(\text{NbTa})_{0.67}(\text{HfZrTi})_{0.33}$  are presented in Figures 3 and 4. The as-milled powders of  $(\text{NbTa})_{0.67}(\text{HfZr})_{0.33}$  formed more compacted, larger

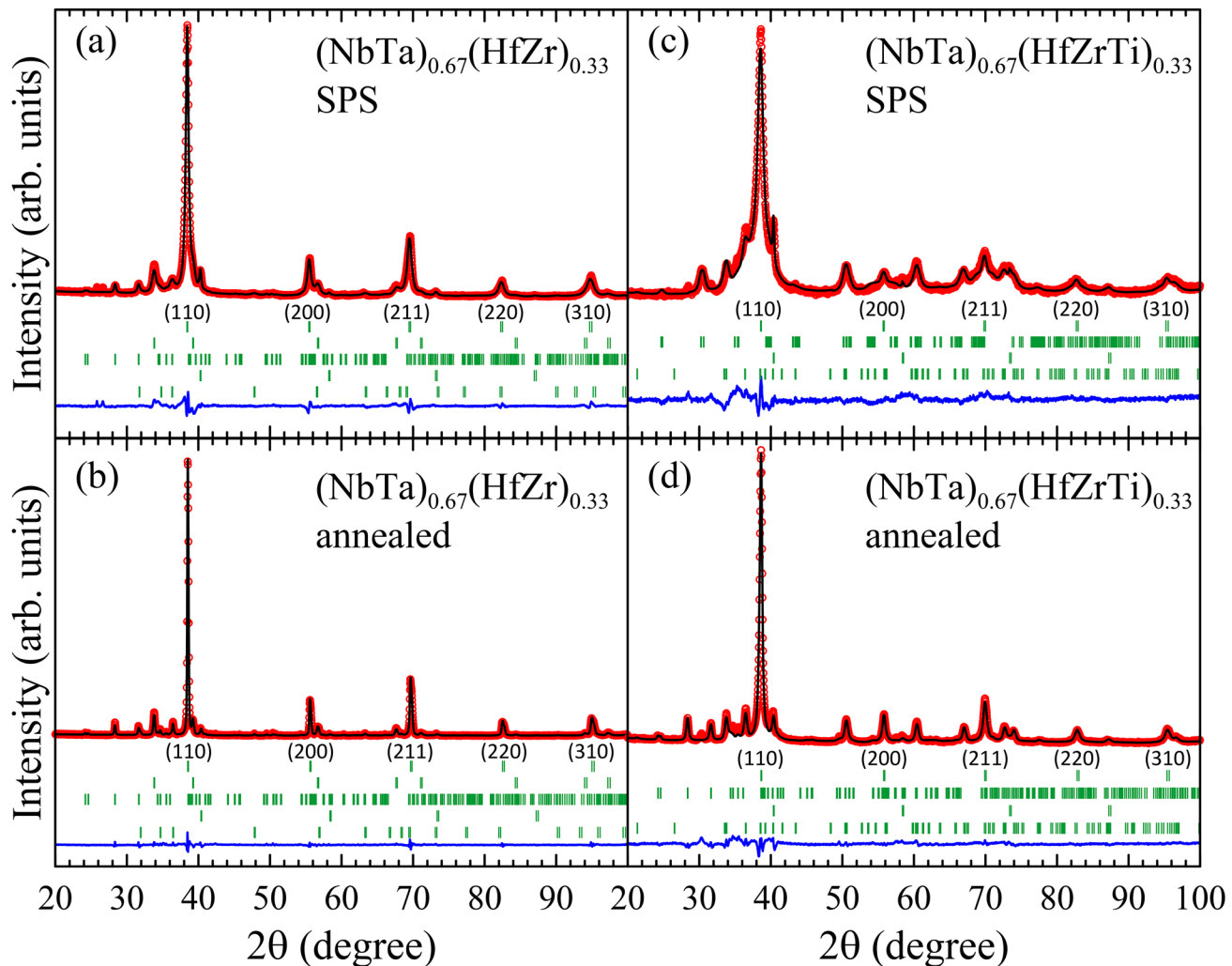


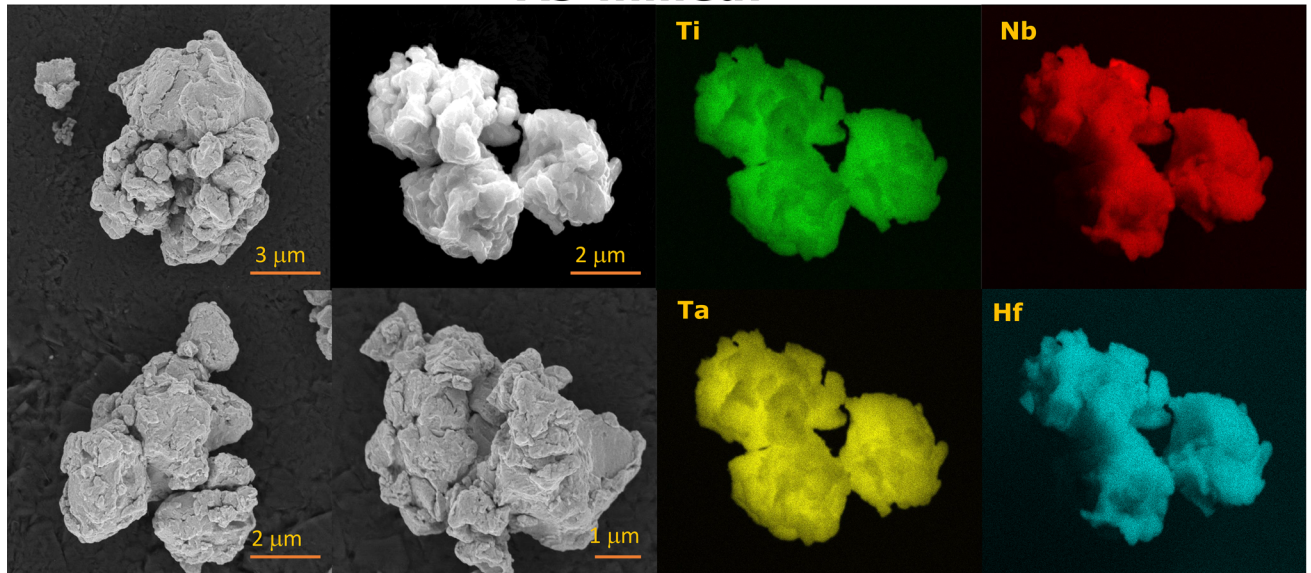
Fig. 2—Powder X-ray diffraction patterns of  $(\text{NbTa})_{0.67}(\text{HfZr})_{0.33}$  powders (a) after SPS process and (b) after annealing in vacuum furnace. Powder X-ray diffraction patterns of  $(\text{NbTa})_{0.67}(\text{HfZrTi})_{0.33}$  powders (c) after SPS process, and (d) after annealing in vacuum furnace. Red dots and black lines represent experimental data and results of the Rietveld refinement, respectively, and blue lines show the difference between the two. Green dashes indicate positions of the Bragg reflections described by the corresponding Miller indices (only for bcc phase) (Color figure online).

agglomerates with lower active surface in comparison to  $(\text{NbTa})_{0.67}(\text{HfZrTi})_{0.33}$  powders. It may be the reason why they are less oxidized. During annealing, the agglomerates of both materials grow in size, but still micrographs of  $(\text{NbTa})_{0.67}(\text{HfZrTi})_{0.33}$  are displaying more loose fragments, which probably corresponds to higher oxides count. Oxides of these elements are expected to have higher optimal sintering temperature than metals. The change in the size of agglomerates of powders after annealing highlights the thermal evolution of the system observed in XRD results. Especially, in  $(\text{NbTa})_{0.67}(\text{HfZr})_{0.33}$ , where after annealing, we can clearly observe the grain boundaries in the agglomerates. It must be noted that at any point after milling, no fractions of the powders were additionally homogenized. Despite that, and despite the results of Rietveld refinements, no visual segregation of the elements is observed on EDXS maps. Taking into account information derived from the Rietveld analysis of the XRD

diffraction patterns, the precipitates must then form randomly distributed agglomerates on submicron scale and thus they can not be clearly distinguished by the EDXS probe. Content of the elements is also in almost perfect agreement with the expected values, as seen in Table I.

The SEM-EDXS micrographs and maps of the SPS-sintered samples (their surfaces) are presented in Figures 5 and 6. Sample  $(\text{NbTa})_{0.67}(\text{HfZr})_{0.33}$  possesses significant amount of small pores which are pointing to fact that optimal sintering conditions have not been reached, but apart of that, sample seems well sintered, homogeneous, and densified. Grain boundaries are not clearly seen. This is in stark difference with morphology of the  $(\text{NbTa})_{0.67}(\text{HfZrTi})_{0.33}$  pellet. For both pellets, the same polishing procedures were applied, but despite that  $(\text{NbTa})_{0.67}(\text{HfZrTi})_{0.33}$  sample retains uneven surface of bulky grains mixed with small ones. In fact, it resembles morphology of annealed  $(\text{NbTa})_{0.67}(\text{HfZrTi})_{0.33}$  powder

## As-milled:



## Annealed:

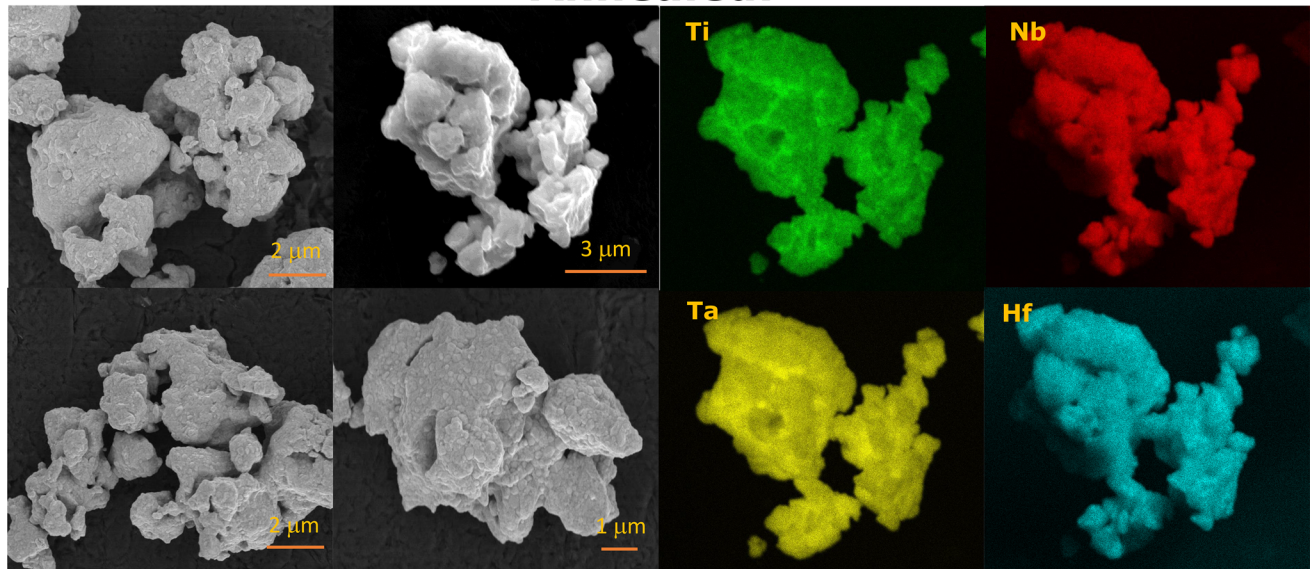


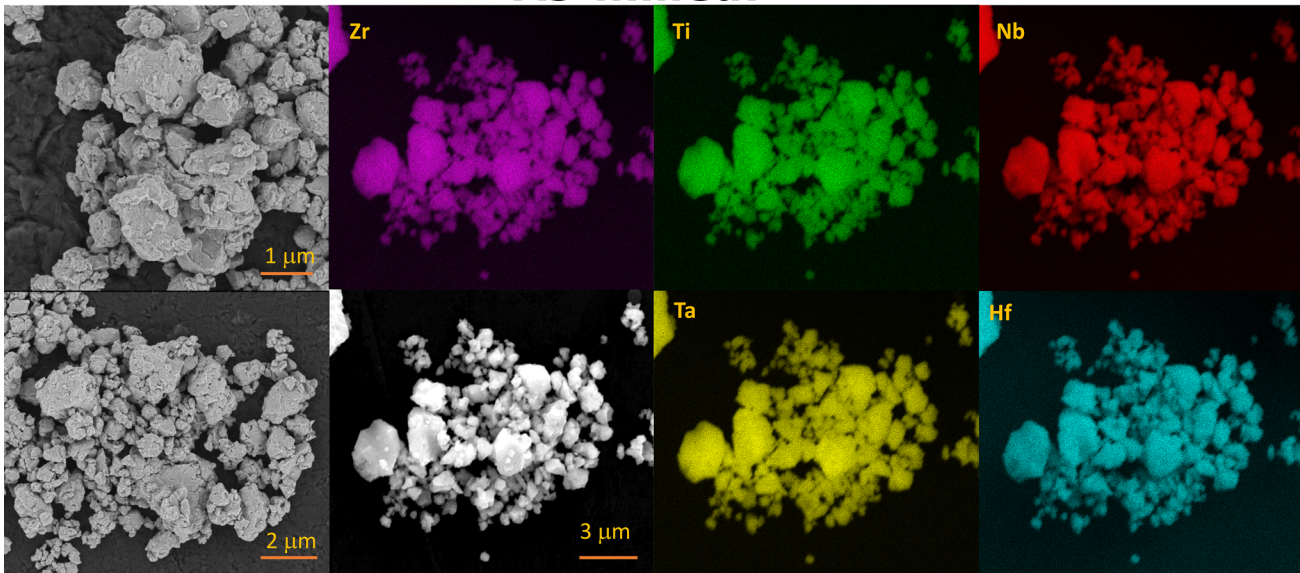
Fig. 3—SEM micrograph and EDXS elemental mapping of the as-milled and annealed  $(\text{NbTa})_{0.67}(\text{HfZr})_{0.33}$  powders.

seen in Figure 4, only additionally pressed. This appearance is most probably due to high oxides content which did not allow sample to be sufficiently densified at 1273 K. It is more similar to a pellet of ceramic or composite than alloy. Despite those morphological differences, medium element content (Table 1) is in very good agreement with both expected values and results for the as-milled, amorphous powders. There are no strong signs of prevalent precipitates or additional structures. Only some spots with higher Hf and Zr content (corresponding to  $\text{ZrO}_2/\text{HfO}_2$  mixed oxide) and some niobium/tantalum-rich spots (that are either connected to oxidized fcc phase or are simply random precipitates) are visible. This type of small precipitates is probably also present in annealed samples (as XRD spectra of both annealed and SPS-sintered samples are showing identical phases). However, due to the

specificity of the SPS process they are segregated better and thus more visible.

The positron annihilation lifetime spectra collected for the as-milled and annealed samples of the  $(\text{NbTa})_{0.67}(\text{HfZr})_{0.33}$  are shown in Figure 7. In the case of the as-milled powder, the PALS spectrum can successfully be described by two components. The first one, characterized by shorter positron mean lifetimes  $\tau_1 = 200(1)$  ps and relative intensity  $I_1 = 81(1)$  pct, describes the free positron annihilation in the studied material. The second one, with  $\tau_s = 396.4$  ps and  $I_s = 19(1)$  pct, is associated with the positron annihilation in the Kapton foil. The determined  $\tau_1$  value can be compared with positron annihilation lifetime data for transition metals presented in works.<sup>[17,18]</sup> For pure metals, which are the components of this powder, the positron bulk lifetimes  $\tau_{bulk}$  are between 120 and 164 ps,

## As-milled:



## Annealed:

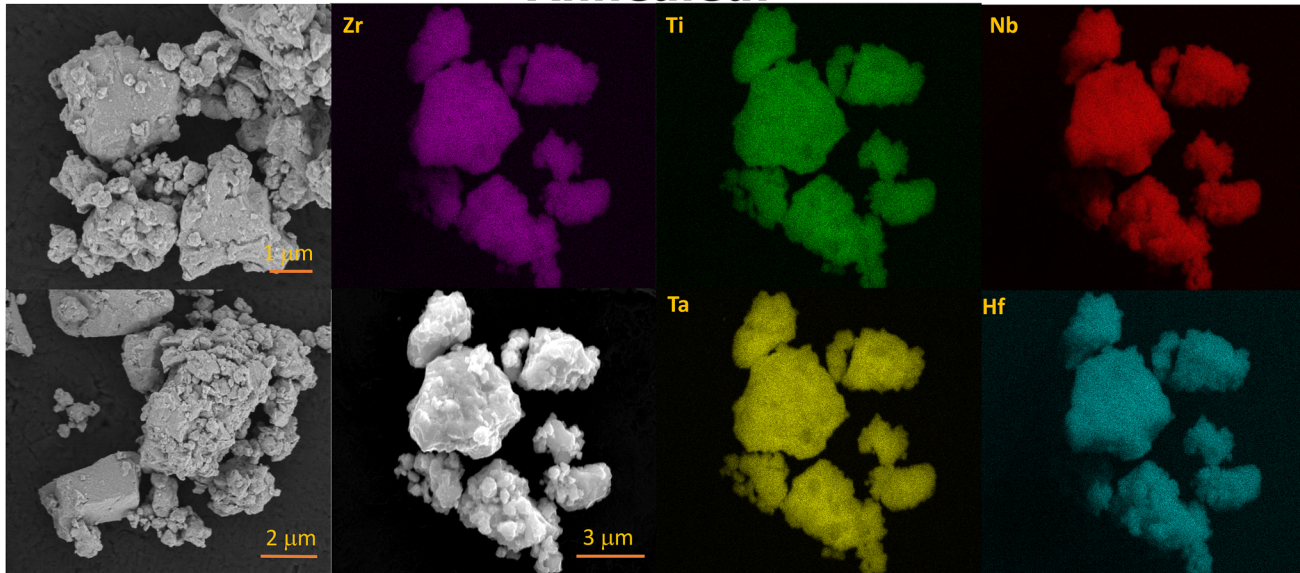


Fig. 4—SEM micrograph and EDXS elemental mapping of the as-milled and annealed  $(\text{NbTa})_{0.67}(\text{HfZrTi})_{0.33}$  powders.

while the positron monovacancy lifetimes  $\tau_{vac}$  are in the range of 203 to 252 ps. As one can notice,  $\tau_1 = 200(1)$  ps is longer than expected  $\tau_{bulk}$  values and shorter than  $\tau_{vac}$ . According to previous studies of amorphous bulk metallic glasses using positron annihilation spectroscopy,<sup>[19–21]</sup> for conventional metallic glasses, the observed positron lifetime value should lie between that for the annealed bulk metals and metal vacancies, since the positrons sample quenched-in regions of open space smaller than a monovacancy. Large-scale variations in the distribution of open space in the amorphous state can lead to a measured annihilation lifetimes that is a weighted average of this distribution. Taking the above into account, one can state that the obtained  $\tau_1 = 200(1)$  ps for as-milled  $(\text{NbTa})_{0.67}(\text{HfZr})_{0.33}$  powder is in agreement with XRD

data which indicates the formation of the amorphous phase during the MA process.

The PALS spectrum measured for annealed  $(\text{NbTa})_{0.67}(\text{HfZr})_{0.33}$  sample can be described using three components with  $\tau_1 = 181(1)$  ps,  $\tau_s = 396.4$  ps, and  $\tau_3 = 2.59(2)$  ns. Their relative intensities are  $I_1 = 74(1)$  pct,  $I_s = 24(1)$  pct, and  $I_3 = 2(1)$  pct. Comparing these values with corresponding data for the as-milled powder, one can notice that  $\tau_1$  decreases significantly by 19 ps and this change is presumably due to crystallization process of amorphous material upon thermal treatment. However, it should be mentioned that  $\tau_1$  is still higher than expected  $\tau_{bulk}$  values for pure Nb, Ta, Zr, and Hf. This may suggest that the crystallized sample contains many phases with a high concentration of positron trap sites, such as dislocations

**Table I. Results of EDXS Measurements of As-Milled Powders of (NbTa)<sub>0.67</sub>(HfZr)<sub>0.33</sub> and (NbTa)<sub>0.67</sub>(HfZrTi)<sub>0.33</sub> and After SPS**

Element (At. Pct)	Nb	Ta	Hf	Zr	Ti
<b>(NbTa)<sub>0.67</sub>(HfZr)<sub>0.33</sub></b>					
Expected	33.5	33.5	16.5	16.5	0
Measured	34.2(± 1.7)	31.8(± 1.5)	16.0(± 1.1)	18.1(± 1.4)	0
<b>(NbTa)<sub>0.67</sub>(HfZrTi)<sub>0.33</sub></b>					
Expected	33.5	33.5	11	11	11
Measured	32.1(± 1.2)	34.5(± 1.2)	11.4(± 0.5)	11.5(± 1.1)	10.5(± 0.7)
<b>(NbTa)<sub>0.67</sub>(HfZr)<sub>0.33</sub> - SPS</b>					
Expected	33.5	33.5	16.5	16.5	0
Measured	33.1(± 2.0)	32.2(± 1.8)	16.6(± 1.2)	18.1(± 1.3)	0
<b>(NbTa)<sub>0.67</sub>(HfZrTi)<sub>0.33</sub> - SPS</b>					
Expected	33.5	33.5	11	11	11
Measured	33.1(± 1.9)	32.1(± 2.3)	10.5(± 1.4)	13.4(± 1.7)	10.9(± 1.8)

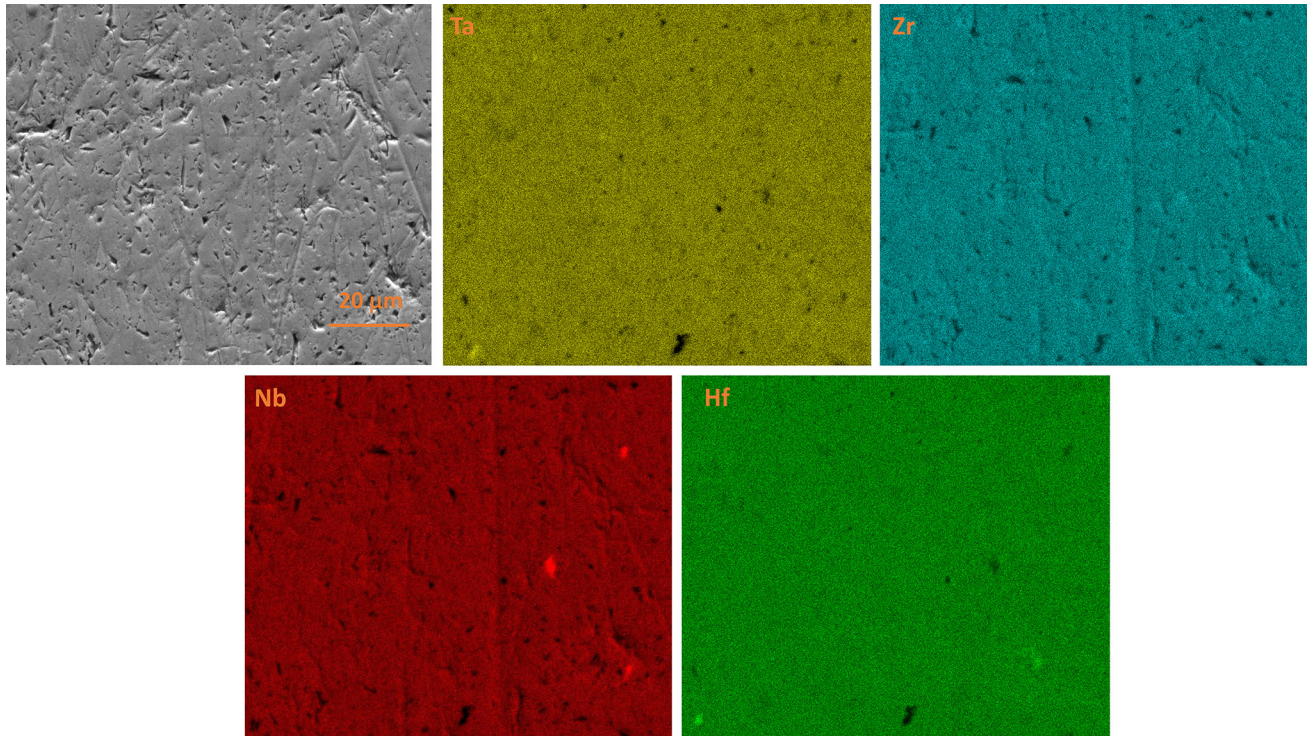


Fig. 5—SEM micrograph and EDXS elemental mapping of the (NbTa)<sub>0.67</sub>(HfZr)<sub>0.33</sub> powder after SPS.

and grain boundaries.<sup>[19,20]</sup> The presence of long-lived component with  $\tau_3 = 2.59(2)$  ns is rather surprising since positron lifetimes longer than 1 ns are generally associated with the pick-off annihilation of orthopositronium (o-Ps) trapped in voids or pores.<sup>[22]</sup> According to the simple Tao-Eldrup model, the relationship between the o-Ps lifetime ( $\tau_3$ ) and the radius  $r$  of the spherical hole is as follows<sup>[23,24]</sup>:

$$\tau_3 = 0.5 \left[ 1 - \frac{r}{r + \Delta r} + \frac{1}{2\pi} \sin\left(\frac{2\pi r}{r + \Delta r}\right) \right]^{-1}, \quad [1]$$

where the factor of 0.5 ns represents the inverse of the spin-averaged Ps annihilation and  $\Delta r = 0.166$  nm is the

depth of the penetration of the Ps-wave function into the walls of the hole. Using this equation,  $r$  close to 0.33 nm is estimated. This finding suggests that the crystallization process of amorphous material upon thermal treatment is also accompanied by formation of relatively large voids which are probably located at interfaces between different crystalline phases.

Figure 8 presents PALS spectra measured for the as-milled and annealed samples of (NbTa)<sub>0.67</sub>(HfZrTi)<sub>0.33</sub>. As one can notice, both spectra can be described with similar models which were used previously to analyze PALS data for (NbTa)<sub>0.67</sub>(HfZr)<sub>0.33</sub>. In particular, the spectrum collected for the as-milled powder consists of two components which correspond

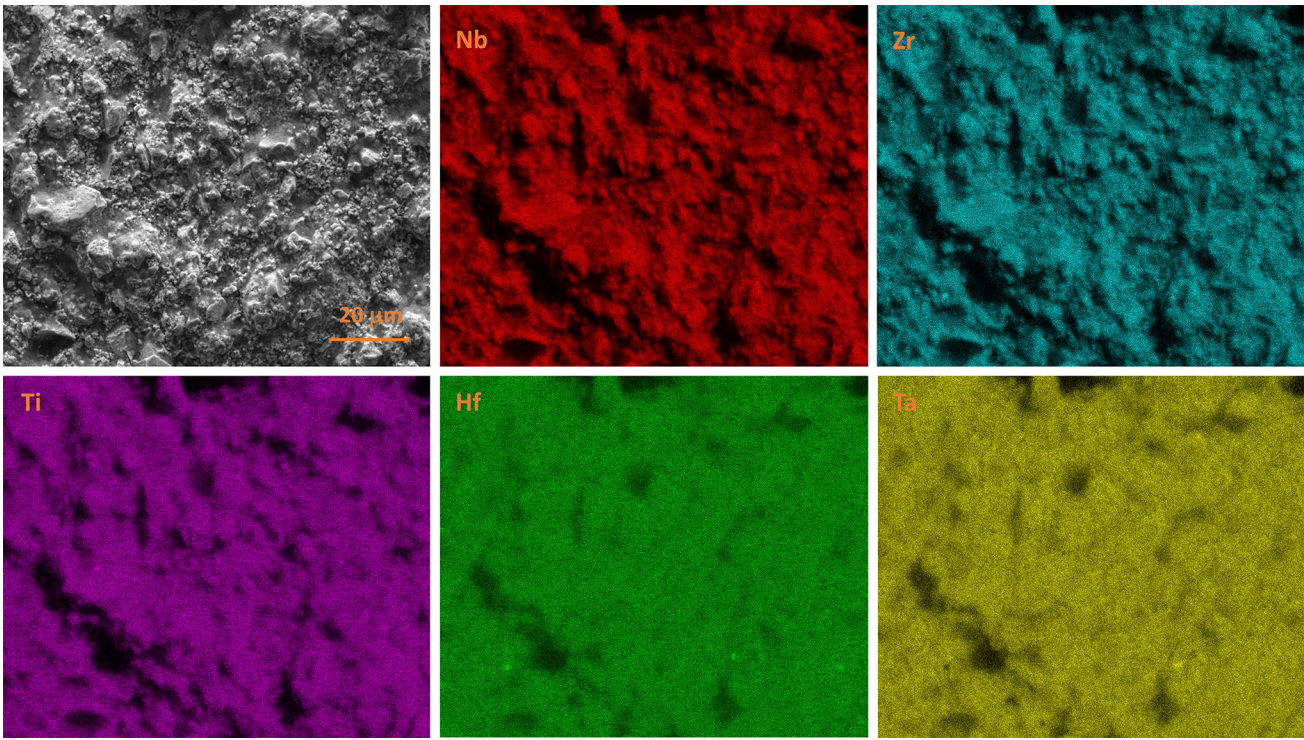


Fig. 6—SEM micrograph and EDXS elemental mapping of the  $(\text{NbTa})_{0.67}(\text{HfZrTi})_{0.33}$  powder after SPS.

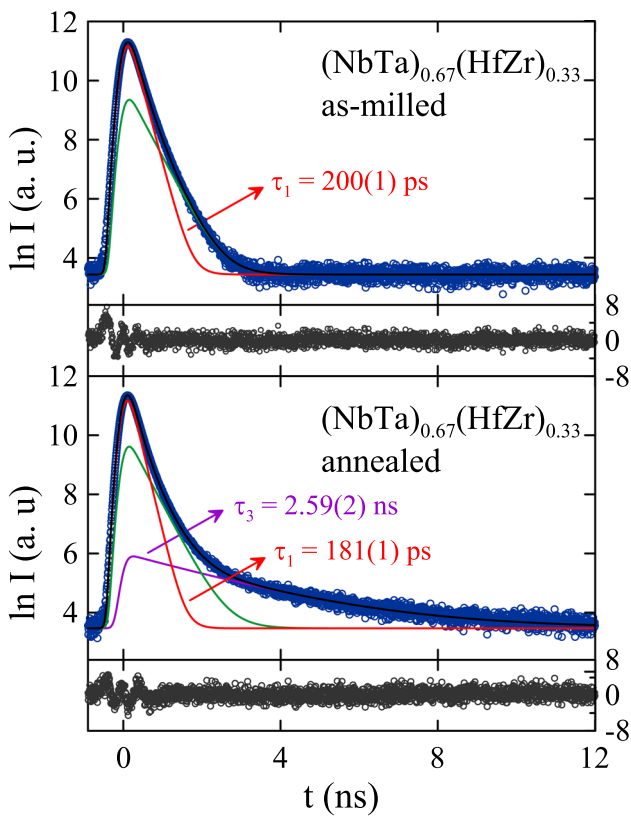


Fig. 7—PALS spectra measured for the as-milled and annealed samples of  $(\text{NbTa})_{0.67}(\text{HfZr})_{0.33}$  (blue open circles) along with fits described in the text (solid curves) and their residuals (black closed circles) (Color figure online).

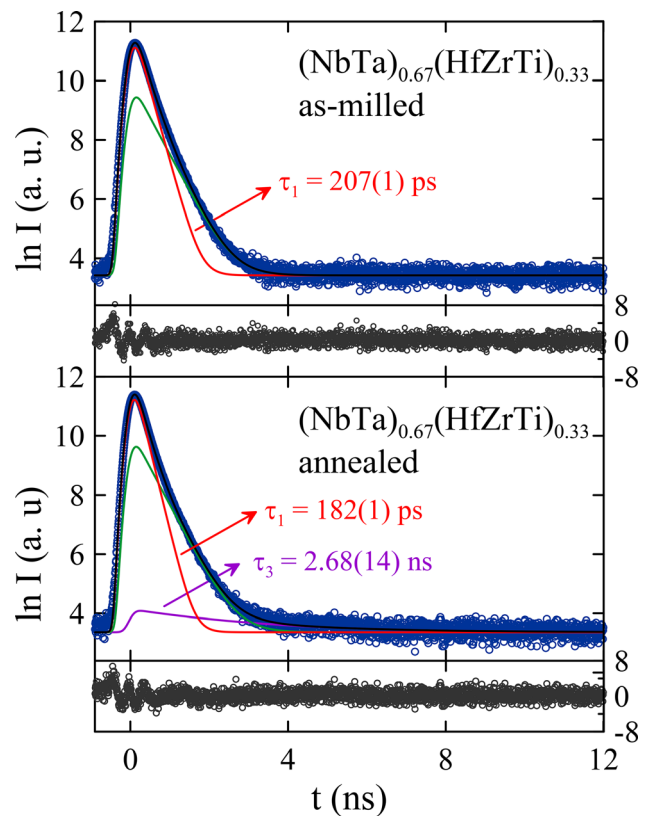


Fig. 8—PALS spectra measured for as-milled and annealed samples of  $(\text{NbTa})_{0.67}(\text{HfZrTi})_{0.33}$  (blue open circles) along with fits described in the text (solid curves) and their residuals (black closed circles) (Color figure online).

to the positron annihilation in studied material ( $\tau_1 = 207(1)$  ps,  $I_1 = 79(1)$  pct) and in the Kapton foil ( $\tau_s = 396.4$  ps,  $I_s = 21(1)$  pct). Accordingly, the spectrum for annealed sample is described using three components with  $\tau_1 = 182(1)$  ps,  $\tau_s = 396.4$  ps, and  $\tau_3 = 2.68(14)$  ns, while their relative intensities are  $I_1 = 76(1)$  pct,  $I_s = 23(1)$  pct, and  $I_3 = 0.2(1)$  pct. It must be noted here that despite the small value of  $I_3$  parameter, the long-lived component is required to reproduce experimental points. Summarizing, the PALS data obtained for  $(\text{NbTa})_{0.67}(\text{HfZrTi})_{0.33}$  samples are in agreement with our previous findings that the as-milled powder is the multicomponent amorphous alloy, while annealing of this system at 1273 K leads to decomposition of the amorphous phase. Finally, it should be mentioned that small differences of  $\tau$  and  $I$  values observed between  $(\text{NbTa})_{0.67}(\text{HfZr})_{0.33}$  and  $(\text{NbTa})_{0.67}(\text{HfZrTi})_{0.33}$  can be connected with different chemical composition of these two systems.

### B. Magnetic and Thermodynamic Properties

According to work,<sup>[5]</sup>  $(\text{NbTa})_{0.67}(\text{HfZr})_{0.33}$  as well as  $(\text{NbTa})_{0.67}(\text{HfZrTi})_{0.33}$  alloys prepared by arc-melting method are conventional type-II superconductors with critical temperatures  $T_c$  close to 6.6 K and 7.6 K, respectively. To compare superconducting properties of the mentioned above systems with our powders prepared by MA, magnetic and specific heat measurements were performed.

Figure 9 presents temperature dependence of mass magnetic susceptibility  $\chi_m$  (left panel) and isothermal field dependence of mass magnetization  $\sigma$  at 1.8 K (right panel) of the as-milled and annealed

$(\text{NbTa})_{0.67}(\text{HfZr})_{0.33}$  powders. In the case of annealed sample, a strong diamagnetic signal below  $T_c = 6.5(3)$  K in  $\chi_m(T)$  is observed, indicating the bulk nature of superconductivity. At the same time,  $\sigma(H)$  data reveal that the annealed sample exhibits type-II superconductivity with the lower critical field  $\mu_0 H_{c1} < 5$  mT and upper critical field  $\mu_0 H_{c2} \approx 1.5$  T. The analysis of XRD patterns collected for this material reveals the presence of five phases. Since the superconducting state was not observed above 2 K for pure W, pure Zr as well as transition metal oxides, the only phase which can be associated with superconductivity in this sample is bcc MEA. Moreover, the estimated critical temperature is in good agreement with  $T_c$  determined previously for  $(\text{NbTa})_{0.67}(\text{HfZr})_{0.33}$  prepared by arc melting.<sup>[5]</sup> A much more intriguing results were obtained for the as-milled powder. As one can notice, both  $\chi_m(T)$  and  $\sigma(H)$  curves display only a very weak diamagnetic signal which cannot be connected with the appearance of bulk superconductivity in the studied powder. In particular, comparing  $\chi_m$  data measured at 25 mT, the value of  $\sim 2 \times 10^{-6} \text{ m}^3 \text{ kg}^{-1}$  obtained at 2 K for the as-milled sample is more than 50 times lower than corresponding value determined for annealed one. Therefore, this finding can be associated with the formation of trace amounts of alloy crystallites in the as-milled powder.

Figure 10 shows  $\chi_m(T)$  (left panel) and  $\sigma(H)$  at 1.8 K (right panel) data measured for the as-milled and annealed  $(\text{NbTa})_{0.67}(\text{HfZrTi})_{0.33}$  samples. The results are comparable with those obtained for  $(\text{NbTa})_{0.67}(\text{HfZr})_{0.33}$ . The annealed sample exhibits bulk superconductivity below 6.6(3) K, while the as-milled powder shows very weak diamagnetic behavior below 7.3(2) K which similarly to  $(\text{NbTa})_{0.67}(\text{HfZr})_{0.33}$  can be

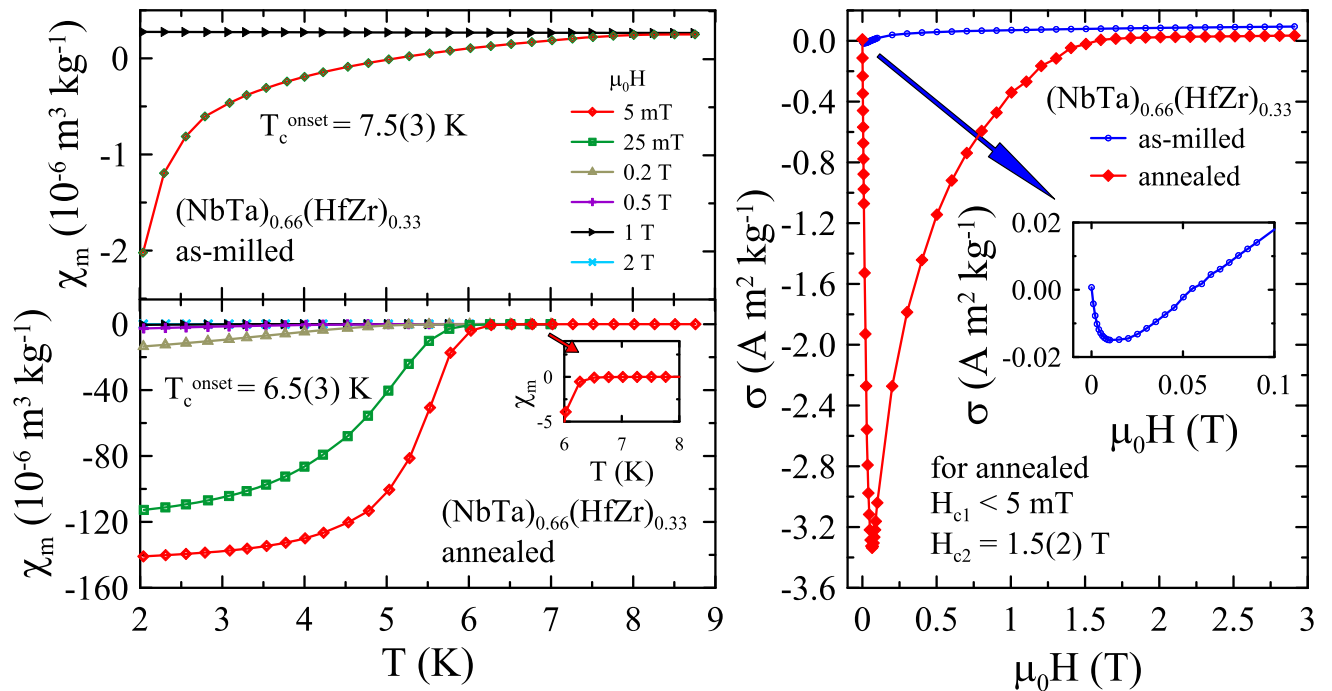


Fig. 9—Temperature dependence of mass magnetic susceptibility  $\chi_m$  of the as-milled and annealed  $(\text{NbTa})_{0.67}(\text{HfZr})_{0.33}$  powders measured in applied magnetic field of  $\mu_0 H = 2$  T (left panel). Isothermal field dependence of mass magnetization  $\sigma$  at 1.8 K (right panel).

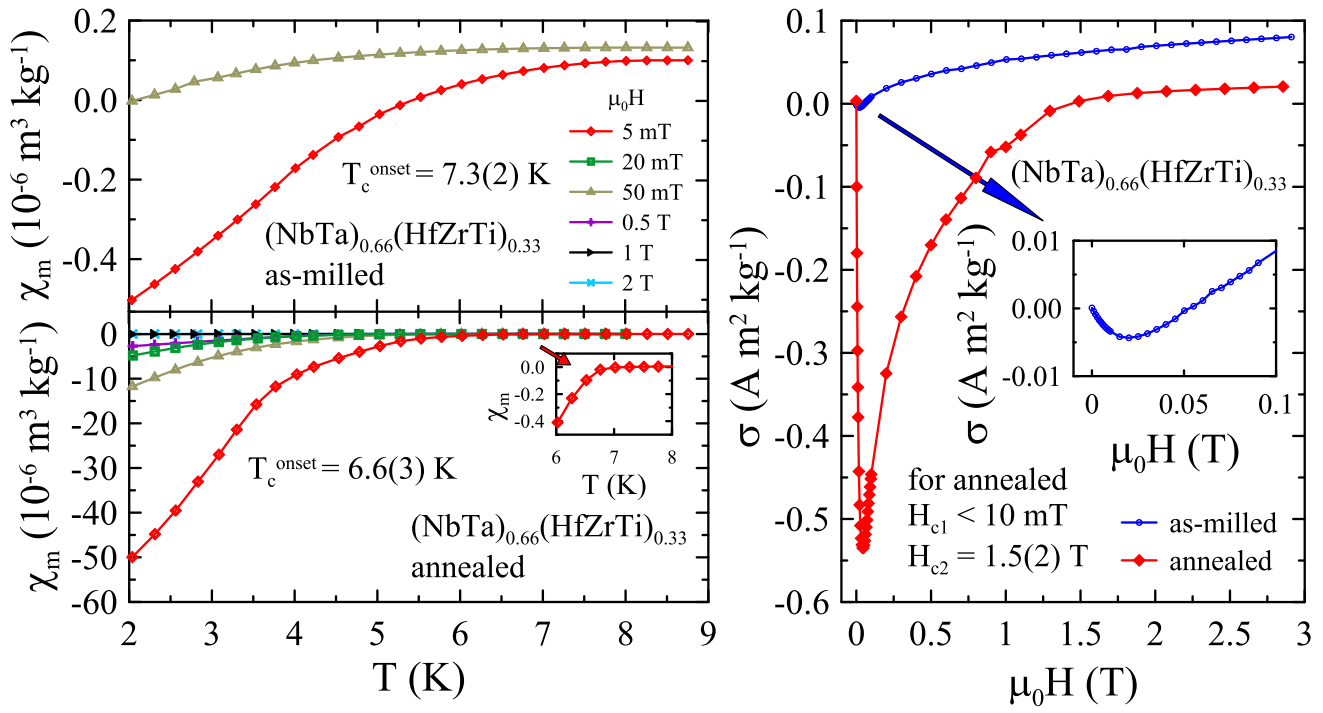


Fig. 10—Temperature dependence of mass magnetic susceptibility  $\chi_m$  of the as-milled and annealed  $(\text{NbTa})_{0.67}(\text{HfZrTi})_{0.33}$  powders measured in applied magnetic field of  $\mu_0 H = 2 \text{ T}$  (left panel). Isothermal field dependence of mass magnetization  $\sigma$  at 1.8 K (right panel).

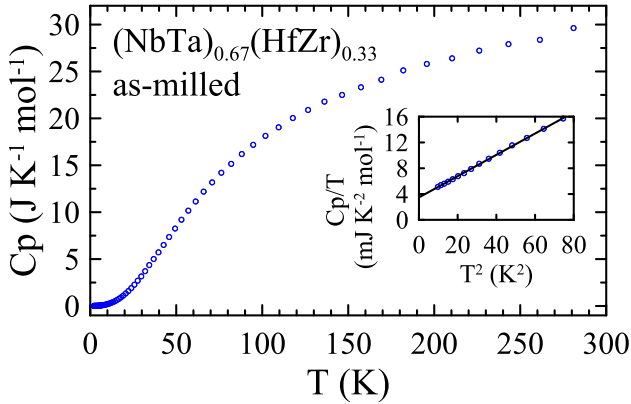


Fig. 11—Specific heat  $C_p(T)$  of the as-milled  $(\text{NbTa})_{0.67}(\text{HfZr})_{0.33}$  pressed into pellet. Inset shows low temperature section of  $C_p/T(T^2)$ . Solid line is a fit to Eq. 2.

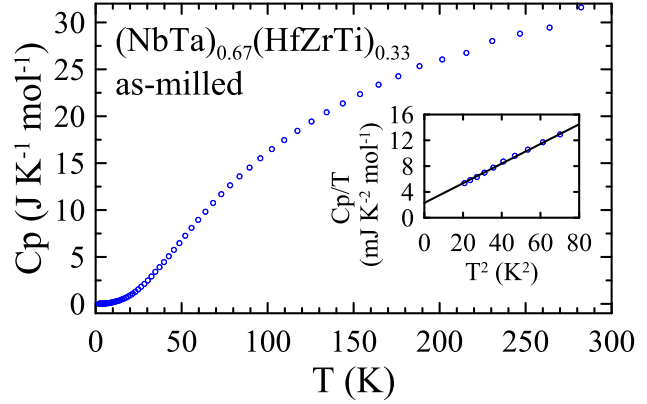


Fig. 12—Specific heat  $C_p(T)$  of the as-milled  $(\text{NbTa})_{0.67}(\text{HfZrTi})_{0.33}$  pressed into pellet. Inset shows low temperature section of  $C_p/T(T^2)$ . Solid line is a fit to Eq. 2.

caused by superconducting bcc alloy particles occurring in the as-milled powder in trace amount.

The temperature dependence of specific heat  $C_p$  of the as-milled samples of  $(\text{NbTa})_{0.67}(\text{HfZr})_{0.33}$  and  $(\text{NbTa})_{0.67}(\text{HfZrTi})_{0.33}$  is presented in Figures 11 and 12. The measurements were performed in temperature range from 2 K to 300 K and without the external magnetic field. As one can notice, both measured curves show no signs of magnetic ordering or superconducting transition, where very weak signals can be seen in magnetic data. At low temperatures,  $C_p/T(T^2)$  experimental data can be described by the equation:

$$C_p(T) = C_{el}(T) + C_{ph}(T) = \gamma T + \beta T^3, \quad [2]$$

where  $C_{el}(T)$  stands for the electron specific heat in the Sommerfeld model,  $C_{ph}(T)$  is the approximation of lattice specific heat in Debye model,  $\gamma$  denotes the Sommerfeld coefficient, and  $\beta$  is the lattice specific heat coefficient. A least-squares fit to this equation is presented in insets of Figures 11 and 12 and gives following results  $\gamma = 3.5(3) \text{ mJ K}^{-2} \text{ mol}^{-1}$  and  $\beta = 0.165(5) \text{ mJ K}^{-4} \text{ mol}^{-1}$  for  $(\text{NbTa})_{0.67}(\text{HfZr})_{0.33}$ , and  $\gamma = 2.3(1) \text{ mJ K}^{-2} \text{ mol}^{-1}$  and  $\beta = 0.15(2) \text{ mJ K}^{-4} \text{ mol}^{-1}$  for  $(\text{NbTa})_{0.67}(\text{HfZrTi})_{0.33}$ .

Using the Sommerfeld coefficient  $\gamma$ , the density of states at Fermi level  $N(E_F)$  can be estimated from following relation:

$$\gamma = \frac{1}{3} \pi^2 k_B^2 N_A N(E_F) \quad [3]$$

yielding 1.5(1) eV<sup>-1</sup>f.u.<sup>-1</sup> for (NbTa)<sub>0.67</sub>(HfZr)<sub>0.33</sub> and 0.9(1) eV<sup>-1</sup>f.u.<sup>-1</sup> for (NbTa)<sub>0.67</sub>(HfZrTi)<sub>0.33</sub>. In Eq. [3],  $k_B$  stands for the Boltzmann constant, while  $N_A$  is the Avogadro number. The calculated  $\gamma$  and  $N(E_F)$  values for the as-milled powders are noticeably lower than corresponding values obtained for well-crystallized (NbTa)<sub>0.67</sub>(HfZrTi)<sub>0.33</sub> alloy synthesized by arc melting where  $\gamma = 7.97(5)$  mJ K<sup>-2</sup> mol<sup>-1</sup> and  $N(E_F) = 1.9$  eV<sup>-1</sup>f.u.<sup>-1</sup>.<sup>[5]</sup> This finding may be connected with our presumption that the as-milled samples are in amorphous or highly disorder state.

In the next step, the obtained  $\beta$  value can be used to calculate the characteristic Debye temperature  $\Theta_D^{LT}$  (the superscript LT indicates that the parameter was estimated from low temperature data) using the following equation:

$$\Theta_D^{LT} = \sqrt[3]{\frac{12\pi^4 r R}{5\beta}}, \quad [4]$$

where  $R$  stands for the universal gas constant and  $r = 1$  is the number of atoms per formula unit. The calculated values of  $\Theta_D^{LT}$  for (NbTa)<sub>0.67</sub>(HfZr)<sub>0.33</sub> and (NbTa)<sub>0.67</sub>(HfZrTi)<sub>0.33</sub> samples are 228(4) K and 234(2) K, respectively.

The magnetic and thermodynamic results obtained for the as-milled (NbTa)<sub>0.67</sub>(HfZr)<sub>0.33</sub> and (NbTa)<sub>0.67</sub>(HfZrTi)<sub>0.33</sub> powders give a clear evidence of the absence of bulk superconductivity in both amorphous multicomponent alloys at temperatures exceeding 2 K. This finding can be taken as an indication that  $T_c$  of amorphous HEAs is lower than those observed in their crystalline counterparts. Moreover, taking into account the valence electron count (VEC) dependence of the superconducting transition temperatures for HEA superconductors as well as for classic amorphous and crystalline alloys which are presented in works,<sup>[5,7]</sup> it can be stated that  $T_c$  of amorphous HEAs could be expected to be lower than observed in amorphous 4d and 5d metals and their amorphous binary alloys.<sup>[25]</sup>

#### IV. CONCLUSIONS

The medium-entropy alloy (NbTa)<sub>0.67</sub>(HfZr)<sub>0.33</sub> and the high-entropy alloy (NbTa)<sub>0.67</sub>(HfZrTi)<sub>0.33</sub> were prepared by mechanical alloying using high-energy planetary ball mill. The obtained XRD, SEM, and PALS data suggest that both the as-prepared powders are multicomponent alloys in amorphous (or highly disordered) state. The absence of strong diamagnetic signal in  $\chi_m(T)$  and  $\sigma(H)$  dependences as well as lack of characteristic peak in  $C_p(T)$  data undoubtedly proves that bulk superconductivity is not observed in both amorphous alloys down to 2 K. At the same time, in (NbTa)<sub>0.67</sub>(HfZr)<sub>0.33</sub> and (NbTa)<sub>0.67</sub>(HfZrTi)<sub>0.33</sub>

powders after SPS sintering or vacuum annealing at 1273 K, the formation of several crystalline phases is observed. Since that it can be concluded that thermal treatment of both studied materials leads to decomposition of the amorphous phase and precipitation of crystalline phases. In both annealed samples, the structure of the main crystalline phase was identified as bcc, and in this phase, bulk superconductivity was observed below 6.5 K.

The absence of bulk superconductivity in both amorphous alloys down to 2 K leads to conclusion that superconducting critical temperatures of amorphous HEAs could be expected to be lower than those observed in their crystalline counterparts as well as in amorphous 4d and 5d metals, and their amorphous binary alloys.

#### ACKNOWLEDGMENTS

This work was financed by the National Science Center (Poland) under the OPUS 20 Project No. 2020/39/B/ST5/01782. For the purpose of Open Access, the authors has applied a CCBY public copyright license to any Author Accepted Manuscript (AAM) version arising from this submission.

#### DATA AVAILABILITY

The data presented in this study are openly available in OSF repository at <https://doi.org/10.17605/OSF.IO/G4N6B>.

#### CONFLICT OF INTEREST

On behalf of all authors, the corresponding author states that there is no conflict of interest.

#### OPEN ACCESS

This article is licensed under a Creative Commons Attribution 4.0 International License, which permits use, sharing, adaptation, distribution and reproduction in any medium or format, as long as you give appropriate credit to the original author(s) and the source, provide a link to the Creative Commons licence, and indicate if changes were made. The images or other third party material in this article are included in the article's Creative Commons licence, unless indicated otherwise in a credit line to the material. If material is not included in the article's Creative Commons licence and your intended use is not permitted by statutory regulation or exceeds the permitted use, you will need to obtain permission directly from the copyright holder. To view a copy of this licence, visit <http://creativecommons.org/licenses/by/4.0/>.

## REFERENCES

1. J.-W. Yeh, S.-K. Chen, S.-J. Lin, J.-Y. Gan, T.-S. Chin, T.-T. Shun, C.-H. Tsau, and S.-Y. Chang: *Adv. Eng. Mater.*, 2004, vol. 6, pp. 299–303. <https://doi.org/10.1002/adem.200300567>.
2. B. Cantor: *Prog. Mater. Sci.*, 2021, vol. 120, p. 100754. <https://doi.org/10.1016/j.pmatsci.2020.100754>.
3. L. Wang, Y. Jiao, R. Liu, D. Wang, Z. Yu, Y. Xi, K. Zhang, S. Xu, H. Liu, L. Wen, X. Xiao, W. Zhang, and J. Ji: *JOM*, 2024, vol. 76, pp. 353–61. <https://doi.org/10.1007/s11837-023-06217-3>.
4. P. Koželj, S. Vrtnik, A. Jelen, S. Jazbec, Z. Jagličić, S. Maiti, M. Feuerbacher, W. Steurer, and J. Dolinšek: *Phys. Rev. Lett.*, 2014, vol. 113, p. 107001. <https://doi.org/10.1103/PhysRevLett.113.107001>.
5. F. Rohr, M.J. Winiarski, J. Tao, T. Klimczuk, and R.J. Cava: *Proc. Natl. Acad. Sci.*, 2016, vol. 113, pp. 7144–50. <https://doi.org/10.1073/pnas.1615926113>.
6. J. Kitagawa, S. Hamamoto, and N. Ishizu: *Metals*, 2020. <https://doi.org/10.3390/met10081078>.
7. L. Sun and R.J. Cava: *Phys. Rev. Mater.*, 2019, vol. 3, p. 090301. <https://doi.org/10.1103/PhysRevMaterials.3.090301>.
8. C. Suryanarayana: *Mater. Res. Lett.*, 2022, vol. 10, pp. 619–47. <https://doi.org/10.1080/21663831.2022.2075243>.
9. A. Kumar, A. Singh, and A. Suhane: *J. Mater. Res. Technol.*, 2022, vol. 17, pp. 2431–56. <https://doi.org/10.1016/j.jmrt.2022.01.141>.
10. J. Rodríguez-Carvajal: *Physica B: Condens. Matter*, 1993, vol. 192, pp. 55–69. [https://doi.org/10.1016/0921-4526\(93\)90108-1](https://doi.org/10.1016/0921-4526(93)90108-1).
11. J. Kansy: *Nucl. Instrum. Methods Phys. Res. Sect. A: Accel. Spectrom. Detect. Assoc. Equip.*, 1996, vol. 374, pp. 235–44. [https://doi.org/10.1016/0168-9002\(96\)00075-7](https://doi.org/10.1016/0168-9002(96)00075-7).
12. R. Idczak, P. Sobota, L.M. Tran, M. Babij, K. Idczak, W. Nowak, and A. Pikul: *Metall. Mater. Trans. A*, 2024, vol. 55A, pp. 523–36. <https://doi.org/10.1007/s11661-023-07263-x>.
13. A. Takeuchi, N. Chen, T. Wada, Y. Yokoyama, H. Kato, A. Inoue, and J.W. Yeh: *Intermetallics*, 2011, vol. 19, pp. 1546–54. <https://doi.org/10.1016/j.intermet.2011.05.030>.
14. H.Y. Ding and K.F. Yao: *J. Non-Cryst. Solids*, 2013, vol. 364, pp. 9–12. <https://doi.org/10.1016/j.jnoncrysol.2013.01.022>.
15. W. Muftah, J. Allport, and V. Vishnyakov: *Surf. Coat. Technol.*, 2021, vol. 422, p. 127486. <https://doi.org/10.1016/j.surfcoat.2021.127486>.
16. X. Feng, C. Feng, and Y. Lu: *Materials*, 2022. <https://doi.org/10.3390/ma15238568>.
17. J.M. Campillo Robles and F. Plazaola: *Defect and Diffusion in Metals. Defect and Diffusion Forum*, vol. 213, Trans Tech Publications Ltd, Baech, 2003, p. 141-0.
18. J.M.C. Robles, E. Ogando, and F. Plazaola: *J. Phys.: Condens. Matter*, 2007, vol. 19, p. 176222. <https://doi.org/10.1088/0953-8984/19/17/176222>.
19. C. Nagel, K. Rätzke, E. Schmidtke, J. Wolff, U. Geyer, and F. Faupel: *Phys. Rev. B*, 1998, vol. 57, pp. 10224–27. <https://doi.org/10.1103/PhysRevB.57.10224>.
20. P. Asoka-Kumar, J. Hartley, R. Howell, P.A. Sterne, and T.G. Nieh: *Appl. Phys. Lett.*, 2000, vol. 77, pp. 1973–75. <https://doi.org/10.1063/1.1313367>.
21. K.M. Flores, D. Suh, R.H. Dauskardt, P. Asoka-Kumar, P.A. Sterne, and R.H. Howell: *J. Mater. Res.*, 2002, vol. 17, pp. 1153–61. <https://doi.org/10.1557/JMR.2002.0171>.
22. Y.C. Jean, P.E. Mallon, and D.M. Schrader: *Principles and Applications of Positron & Positronium Chemistry*, World Scientific, Singapore, 2003.
23. S.J. Tao: *J. Chem. Phys.*, 2003, vol. 56, pp. 5499–510. <https://doi.org/10.1063/1.1677067>.
24. M. Eldrup, D. Lightbody, and J.N. Sherwood: *Chem. Phys.*, 1981, vol. 63, pp. 51–58. [https://doi.org/10.1016/0301-0104\(81\)80307-2](https://doi.org/10.1016/0301-0104(81)80307-2).
25. M.M. Collver and R.H. Hammond: *Phys. Rev. Lett.*, 1973, vol. 30, pp. 92–95. <https://doi.org/10.1103/PhysRevLett.30.92>.

**Publisher's Note** Springer Nature remains neutral with regard to jurisdictional claims in published maps and institutional affiliations.